

The close classical T Tauri binary V4046 Sgr: Complex magnetic fields & distributed mass accretion.

J.-F. Donati^{1*}, S.G. Gregory², T. Montmerle^{3,4}, A. Maggio⁵, C. Argiroff^{6,5},
G. Sacco⁷, G. Hussain⁸, J. Kastner⁷, S.H.P. Alencar⁹, M. Audard¹⁰, J. Bouvier⁴,
F. Damiani⁵, M. Güdel¹¹, D. Huenemoerder¹², G.A. Wade¹³

¹ IRAP–UMR 5277, CNRS & Univ. de Toulouse, 14 Av. E. Belin, F–31400 Toulouse, France

² California Institute of Technology, MC 249-17, Pasadena, CA 91125, USA

³ Institut d’Astrophysique de Paris, 98bis Bd Arago, F–75014 Paris, France

⁴ IPAG–UMR 5274, CNRS & Univ. J. Fourier, 414 rue de la Piscine, F–38041 Grenoble, France

⁵ INAF, Osservatorio Astronomico di Palermo, Piazza del Parlamento 1, 90134 Palermo, Italy

⁶ Dip. di Fisica, Univ. di Palermo, Piazza del Parlamento 1, 90134 Palermo, Italy

⁷ Center for Imaging Science, Rochester Institute of Technology, 54 Lomb Memorial Drive, Rochester, NY 14623, USA

⁸ ESO, Karl-Schwarzschild-Str. 2, D-85748 Garching, Germany

⁹ Departamento de Física – ICEx – UFMG, Av. Antônio Carlos, 6627, 30270-901 Belo Horizonte, MG, Brazil

¹⁰ ISDC Data Center for Astrophysics, University of Geneva, Ch. d’Ecogia 16, 1290 Versoix, Switzerland

¹¹ Department of Astronomy, University of Vienna, Trkenschanzstr. 17, 1180 Vienna, Austria

¹² Massachusetts Institute of Technology, Kavli Institute for Astrophysics and Space Research, 70 Vassar St., Cambridge, MA 02139, USA

¹³ Department of Physics, Royal Military College of Canada, PO Box 17000, Station Forces, Kingston, Ontario K7K 7B4, Canada

2011 April, MNRAS submitted

ABSTRACT

We report here the first results of a multi-wavelength campaign focussing on magnetospheric accretion processes within the close binary system V4046 Sgr, hosting two partly-convective classical T Tauri stars of masses $\simeq 0.9 M_{\odot}$ and age $\simeq 12$ Myr. In this paper, we present time-resolved spectropolarimetric observations collected in 2009 September with ESPaDOnS at the Canada-France-Hawaii Telescope (CFHT) and covering a full span of 7 d or $\simeq 2.5$ orbital/rotational cycles of V4046 Sgr. Small circularly polarised Zeeman signatures are detected in the photospheric absorption lines but not in the accretion-powered emission lines of V4046 Sgr, thereby demonstrating that both system components host large-scale magnetic fields weaker and more complex than those of younger, fully-convective cTTs of only a few Myr and similar masses.

Applying our tomographic imaging tools to the collected data set, we reconstruct maps of the large-scale magnetic field, photospheric brightness and accretion-powered emission at the surfaces of both stars of V4046 Sgr. We find that these fields include significant toroidal components, and that their poloidal components are mostly non-axisymmetric with a dipolar component of 50–100 G strongly tilted with respect to the rotation axis; given the similarity with fields of partly-convective main-sequence stars of similar masses and rotation periods, we conclude that these fields are most likely generated by dynamo processes. We also find that both stars in the system show cool spots close to the pole and extended regions of low-contrast, accretion-powered emission; it suggests that mass accretion is likely distributed rather than confined in well defined high-contrast accretion spots, in agreement with the derived magnetic field complexity.

Key words: stars: magnetic fields – stars: formation – stars: imaging – stars: rotation – stars: binary – stars: individual: V4046 Sgr – techniques: polarimetric

1 INTRODUCTION

From the collapse of giant molecular clouds to their fragmentation into individual stars and their planetary systems,

* E-mail: donati@ast.obs-mip.fr

from the dissipation of the initial cloud angular momentum content to the generation of outflows and jets, magnetic fields have a strong impact on most physical processes involved in the formation of stars and planets and are now clearly recognized as one of the few main ingredients (along with gravitation and turbulence) in Nature's recipe to build new worlds (e.g., André et al. 2009; Donati & Landstreet 2009). In the latter formation phases in particular, low-mass Sun-like stars young enough to be still surrounded by, and accreting mass from, a gaseous disc (the classical T Tauri stars or cTTSs) are apparently capable of generating and sustaining a large-scale magnetic field through dynamo processes, which in turn manages to disrupt the inner disc regions and drastically brake the rotation of the central protostar (see, e.g., Bouvier et al. 2007a, for a review).

The presence of intense magnetic fields at the surfaces of cTTSs, and more generally of all T Tauri stars, was first derived through indirect proxies (i.e., continuum or line emission throughout the whole electromagnetic spectrum, from the radio to X-rays, e.g., Feigelson & Montmerle 1999; Favata & Micela 2003; Güdel & Nazé 2009, for reviews), then demonstrated directly (through the Zeeman broadening of spectral lines) about 2 decades ago (e.g., Johns-Krull 2007, for an overview). However, the actual large-scale magnetic topologies of cTTSs - a crucial parameter to elucidate the way such fields manage to couple the protostars to their discs, to funnel the accreted disc material to the stellar surface, and to strongly brake the rotation of the protostar - remained rather elusive until recently. Through spectropolarimetric observations consisting of time-series of Zeeman signatures from accreting and non-accreting regions at the surfaces of cTTSs, new studies demonstrated that very young low-mass stars indeed host large-scale fields of dynamo origin, whose topologies are reminiscent of those of main-sequence stars (once differences in the internal stellar structures are taken into account).

This new opportunity offers the option of investigating magnetospheric accretion processes of cTTSs in a much more global and consistent way, by carrying out simultaneously observations of selected prototypical cTTSs with as wide a spectral coverage as possible, and including in particular the X-ray and optical domains. While optical lines provide information on the large-scale magnetosphere and on the location and rate at which mass is accreted from the disc to the surface of the protostar, high resolution X-ray spectra (and in particular the softer component) yields key material on the shock that occurs when the accretion flows collide with the high atmosphere of the protostar. The present study takes place in the framework of an international multi-wavelength, multi-site campaign organised on V4046 Sgr, one of the few known close cTTS binaries and one of the best cases where the softer component of the X-ray spectrum (attributable to magnetospheric accretion shocks) can be recorded with sufficient accuracy (Günther et al. 2006). This campaign was triggered by a Large Program with XMM-Newton, aimed at obtaining phase-resolved X-ray observations of V4046 Sgr covering about 2 consecutive orbital/rotation cycles of the cTTS binary (for a total exposure time of $\simeq 370$ ks).

Spectropolarimetric (optical) observations of V4046 Sgr were also scheduled in conjunction with (though slightly before than) the main X-ray program, and were carried out in

a way similar to those achieved in the framework of the international MaPP (Magnetic Protostars and Planets) project. Through a survey of a dozen cTTSs, MaPP investigates how the large-scale magnetic fields of low-mass protostars depend on stellar parameters such as mass, age, rotation and accretion rates (e.g., Donati et al. 2010, 2011a); MaPP also includes a theoretical component aiming at describing consistently (through analytical modelling and numerical simulations) how magnetic fields of cTTSs couple to their surrounding accretion disc, how they channel accretion into discrete funnels and what is the resulting angular momentum evolution (see, e.g., Gregory et al. 2010, for an extensive review on the subject). At this stage, however, MaPP has only focussed on single (or distant binary) stars and has not addressed the specific issue of magnetospheric accretion processes in close binary stars; the present campaign on V4046 Sgr thus appears as a worthwhile and timely complement to the core MaPP program.

The complete results of the V4046 Sgr project will be published in a series of papers, starting with a global overview of the campaign and a summary of the main X-ray results (Argiroffi et al. 2011, submitted). The present paper belongs to this series and aims at obtaining, for both cTTSs forming the close V4046 Sgr binary, observational constraints similar to those recently derived for single cTTSs; in particular, it aims at simultaneously deriving the large-scale magnetic fields of both stars of V4046 Sgr, their photospheric brightness maps and their chromospheric distributions of accretion-induced hot spots. Companion papers (e.g., Maggio et al. 2011, Sacco et al. 2011, in preparation) describe additional data sets collected during the same campaign.

After summarising the main characteristics of the close V4046 Sgr cTTS binary (Sec. 2), we describe the new spectropolarimetric observations we collected and outline the associated temporal variability and rotational modulation (Secs. 3 and 4). We then detail the modelling of these data with our magnetic imaging code (Sec. 5) and briefly compare our results with those already published for single cTTSs and with the predictions of the latest numerical simulations of accretion from circumbinary discs in close cTTS binaries (Sec. 6).

2 V4046 SGR (HDE 319139, HBC 662, AS 292)

Located at a distance of about 73 pc, V4046 Sgr is a likely member of the nearby loose β Pic association (Torres et al. 2008). It is one of the few known close cTTS binaries, showing signs of accretion typical of single cTTSs (e.g., large and variable H α emission). It is a double line spectroscopic binary with a circular orbit, a rather short orbital period ($\simeq 2.42$ d) and a prominent excess at IR and radio frequencies indicating the presence of a circumbinary accretion disc (with an inner radius of 0.2–0.4 AU and extending out to several hundred AUs, Quast et al. 2000; Rodríguez et al. 2010). The photometric and spectroscopic periods are equal and demonstrate that the system is synchronised, as expected for a binary system as close as V4046 Sgr. Given that V4046 Sgr has already completed both circularisation and synchronisation, we can logically assume that the or-

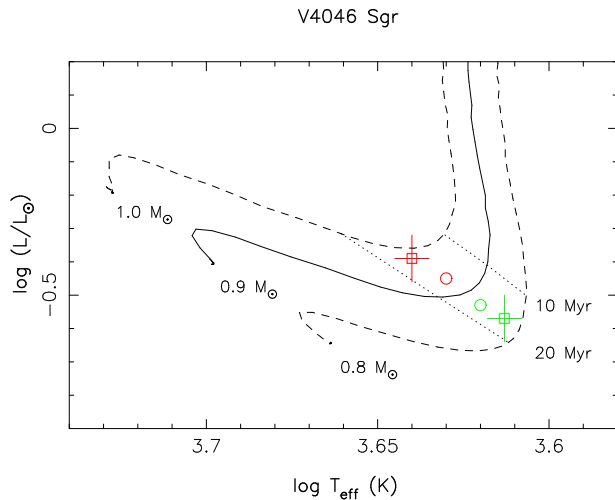


Figure 1. Observed (open squares and error bars) location of the primary (red) and secondary (green) components of V4046 Sgr in the HR diagram, as derived from their respective temperatures and radii (see text). The best match to these positions when further imposing a primary-to-secondary mass ratio of 1.06 (as derived from the velocity curves) is also indicated (open circles). The PMS evolutionary tracks and corresponding isochrones (Siess et al. 2000) assume solar metallicity and include convective overshooting.

bital and rotation axes are aligned, following predictions of the tidal theory (e.g., Hut 1981; Zahn & Bouchet 1989).

Two different detailed spectroscopic studies of V4046 Sgr are available from the literature (Quast et al. 2000; Stempels & Gahm 2004). From the photometric colors, velocity amplitudes and the wavelength-dependent primary-to-secondary magnitude contrast, these studies show in particular that both system components have similar masses and surface temperatures of about $0.9 M_{\odot}$ and 4250 K, the primary being about 6% more massive and 250 K hotter than the secondary. The system is seen mostly pole-on, with an angle between the orbital axis and the line of sight of $\simeq 35^{\circ}$ (Quast et al. 2000; Rodriguez et al. 2010). The line-of-sight-projected equatorial rotation velocities $v \sin i$ that we estimate for both system components (equal to 13.5 ± 0.5 and $12.5 \pm 0.5 \text{ km s}^{-1}$ for the primary and secondary stars respectively) agree with previous estimates and indicate respective radii of 1.12 ± 0.05 and $1.04 \pm 0.05 R_{\odot}$. The position of both stars in the HR diagram (as derived from the above temperatures and radii) and their relative locations with respect to the theoretical evolutionary tracks and isochrones of Siess et al. (2000), shown in Fig. 1, suggest an age of $\simeq 15$ Myr; this is in agreement with recent age estimates of the β Pic moving group as a whole (ranging from 10 to 20 Myr, e.g., Mentuch et al. 2008; da Silva et al. 2009; Yee & Jensen 2010) and in particular with the widely accepted and quoted age of 12 Myr (Torres et al. 2008). It indicates that V4046 Sgr is approaching the end of the TTS stage; at this age, both stars should be partly convective, with the convective zone occupying the outer $\simeq 50\%$ of the stellar radius (Siess et al. 2000).

The distance between both components as derived from the semi-amplitude of the velocity curves (found to be 51.4 ± 0.2 and $54.3 \pm 0.2 \text{ km s}^{-1}$ from our data) is $8.8 R_{\odot}$ or 0.041 AU , in good agreement with the results of Quast et al.

(2000). However, the system velocity that we derive ($-5.7 \pm 0.2 \text{ km s}^{-1}$, see Sec. 5) is significantly different from the former estimate (e.g., $-6.94 \pm 0.16 \text{ km s}^{-1}$ Quast et al. 2000) and suggests that the system also hosts a third distant component. The very precise radial velocity (RV) of the circumbinary (CO disc) material (equal to $-6.21 \pm 0.01 \text{ km s}^{-1}$ in the heliocentric frame, Rodriguez et al. 2010) confirms that this is likely the case.

X-ray spectra of V4046 Sgr with Chandra-HETGS clearly show He-like triplets with line strength ratios in agreement with the predictions of magnetospheric accretion models, confirming that V4046 Sgr is still accreting mass from the surrounding disc (Günther et al. 2006). From the equivalent widths and the corresponding line fluxes of the optical emission lines usually considered as good accretion proxies (and in particular the He I D_3 line and the Ca II infrared triplet, IRT) and using the published empirical correlations between lines and accretion fluxes (Fang et al. 2009), we can derive an estimate of the average logarithmic mass accretion rate (in $M_{\odot} \text{ yr}^{-1}$) at the surface of each star of V4046 Sgr, that we find to be equal to -9.3 ± 0.3 (assuming both stars have equal accretion rates) in agreement with independent estimates from optical proxies (Curran et al. 2011). As usual, this is larger than the estimate derived from X-ray data (equal to -9.84 ± 0.11 for V4046 Sgr, Curran et al. 2011). Optical veiling, i.e., the apparent weakening of the photospheric spectrum (presumably caused by accretion) is apparently weak for V4046 Sgr (e.g., Stempels & Gahm 2004).

V4046 Sgr shares similarities with another member of the β Pic moving group, the young pre-main-sequence close binary HD 155555 (Dunstone et al. 2008; Yee & Jensen 2010), whose stars are slightly more massive ($1.1\text{--}1.2 M_{\odot}$), larger ($\simeq 1.3 R_{\odot}$), warmer ($\simeq 5500 \text{ K}$) and closer to each other (0.036 AU); both systems are thus structurally alike though different regarding their accretion properties and related issues, HD 155555 having dissipated its accretion disc already. HD 155555 may thus serve as a convenient check to identify what in V4046 Sgr is typical of young partly-convective Sun-like binaries and what is more specific to cTTS binaries.

3 OBSERVATIONS

Spectropolarimetric observations of V4046 Sgr were collected from 2009 September 03 to 09 using ESPaDOnS on the CFHT. ESPaDOnS collects stellar spectra spanning the whole optical domain (from 370 to 1,000 nm) at a resolving power of 65,000 (i.e., 4.6 km s^{-1}) and with a spectral sampling of 2.6 km s^{-1} , in either circular or linear polarisation (Donati 2003). A total of 8 circular polarisation spectra were collected over a timespan of 7 consecutive nights. All polarisation spectra consist of 4 individual subexposures each lasting 390 s and taken in different polarimeter configurations to allow the removal of all spurious polarisation signatures at first order.

All raw frames are processed with LIBRE ESPRIT, a fully automatic reduction package/pipeline available at CFHT. It automatically performs optimal extraction of ESPaDOnS unpolarized (Stokes I) and circularly polarized (Stokes V) spectra grossly following the procedure described

Table 1. Journal of observations collected in 2009 September. Columns 1–4 respectively list the UT date, the heliocentric Julian date and UT time (both at mid-exposure), and the peak signal to noise ratio (per 2.6 km s^{-1} velocity bin) of each observation (i.e., each sequence of $4 \times 390 \text{ s}$ subexposures). Column 5 lists the rms noise level (relative to the unpolarized continuum level I_c and per 1.8 km s^{-1} velocity bin) in the circular polarization profile produced by Least-Squares Deconvolution (LSD), while column 6 indicates the orbital/rotational cycle associated with each exposure (using the ephemeris given by Eq. 1).

Date	HJD (2,455,000+)	UT (h:m:s)	S/N	σ_{LSD} ($10^{-4} I_c$)	Cycle (3336+)
Sep 03	77.77383	06:33:30	180	2.9	0.755
Sep 04	78.81648	07:35:02	170	2.6	1.186
Sep 05	79.72103	05:17:41	200	2.1	1.560
Sep 06	80.72065	05:17:14	200	2.1	1.972
Sep 06	80.81321	07:30:32	210	1.9	2.011
Sep 07	81.72152	05:18:36	160	2.5	2.386
Sep 08	82.72171	05:18:60	200	2.0	2.799
Sep 09	83.72107	05:18:11	210	1.8	3.212

in Donati et al. (1997). The velocity step corresponding to CCD pixels is about 2.6 km s^{-1} ; however, thanks to the fact that the spectrograph slit is tilted with respect to the CCD lines, spectra corresponding to different CCD columns across each order feature a different pixel sampling. LIBRE ESPRIT uses this opportunity to carry out optimal extraction of each spectrum on a sampling grid denser than the original CCD sampling, with a spectral velocity step set to about 0.7 CCD pixel (i.e. 1.8 km s^{-1}). All spectra are automatically corrected of spectral shifts resulting from instrumental effects (e.g., mechanical flexures, temperature or pressure variations) using telluric lines as a reference. Though not perfect, this procedure provides spectra with a relative RV precision of better than 0.030 km s^{-1} (e.g., Donati et al. 2008a).

The peak signal-to-noise ratios (S/N, per 2.6 km s^{-1} velocity bin) achieved on the collected spectra (i.e., the sequence of 4 subexposures) range between 160 and 210 depending on weather/seeing conditions, with a median of 200.

Following Stempels & Gahm (2004), orbital/rotational cycles E are computed from heliocentric Julian dates according to the ephemeris:

$$\text{HJD} = 2446998.335 + 2.4213459E \quad (1)$$

We however note that the time of first conjunction (with the primary component in front) in our data is significantly shifted with respect to the ephemeris predictions and occurs at phase 0.681^1 instead of phase 0.75 (i.e., 0.069 cycle or about 4 hr ahead of time). The origin of this shift is not fully clear yet. It can reflect a slightly overestimated orbital period; if this is the case, the orbital period needs to be updated to $2.421296 \pm 0.000001 \text{ d}$, i.e., a value smaller than those of Quast et al. (2000) and of Stempels & Gahm (2004) by 9 and 12 of their σ (0.000004 d) respectively. It may also potentially reflect (at least partly) temporal fluc-

¹ The epoch of first quadrature as derived from our observations occurs on $\text{HJD} = 2455078.199 \pm 0.001 \text{ d}$, with one of our spectra collected very shortly after second conjunction (on Sep 04).

V4046 Sgr, LSD profiles, 2009 Sep 06

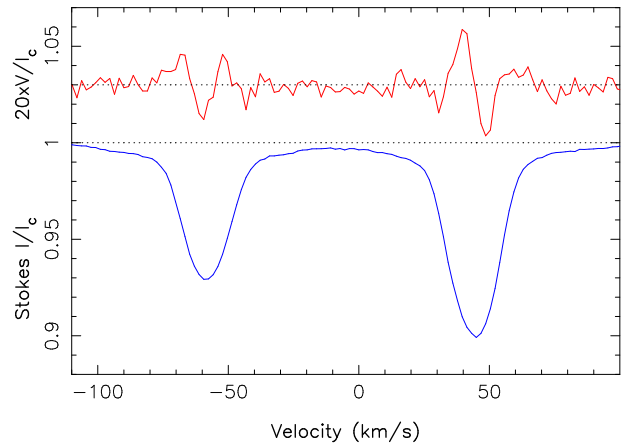


Figure 2. LSD circularly-polarized (Stokes V) and unpolarized (Stokes I) profiles of V4046 Sgr (top/red, bottom/blue curves respectively) collected on 2009 September 06 (cycle 1.972), i.e., slightly after first quadrature (occurring at phase 0.931, see Sec. 3). Zeeman signatures are clearly detected in the LSD profiles of both the primary (right) and secondary (left) system components. The mean polarization profile is expanded by a factor of 20 and shifted upwards by 1.03 for display purposes.

tuations of the orbital period, either caused by a light-time effect (e.g., that induced by the distant third body causing the RV changes mentioned in Sec. 2) and/or by changes in the quadrupolar moments of both components of V4046 Sgr (resulting from activity cycles of one or both system components and known as the Applegate effect, Applegate 1992; Lanza 2006). This issue will be specifically addressed in more details in a forthcoming paper.

Least-Squares Deconvolution (LSD, Donati et al. 1997) was applied to all observations. The line list we employed for LSD is computed from an ATLAS9 LTE model atmosphere (Kurucz 1993) and corresponds to a K5V spectral type ($T_{\text{eff}} = 4,250 \text{ K}$ and $\log g = 4.5$) appropriate for V4046 Sgr. Only moderate to strong atomic spectral lines (with line-to-continuum core depressions larger than 40% prior to all non-thermal broadening) are included in this list; spectral regions with strong lines mostly formed outside the photosphere (e.g., Balmer, He, Ca II H, K and IRT lines) and/or heavily crowded with telluric lines were discarded. Altogether, about 8,000 spectral features (with about 40% from Fe I) are used in this process. Expressed in units of the unpolarized continuum level I_c , the average noise levels of the resulting Stokes V LSD signatures are ranging from 1.8 to 2.9×10^{-4} per 1.8 km s^{-1} velocity bin.

The full journal of observations is presented in Table 1.

4 SPECTROSCOPIC VARIABILITY

Before applying our tomographic imaging tools to the V4046 Sgr data, it is usually worthwhile to examine how spectral lines (and in particular the equivalent widths, RVs and the average magnetic fluxes) vary with rotation cycle throughout the observing run; at the very least, it provides a rough, intuitive understanding of how the large-scale field is structured and oriented, and where the cool photospheric

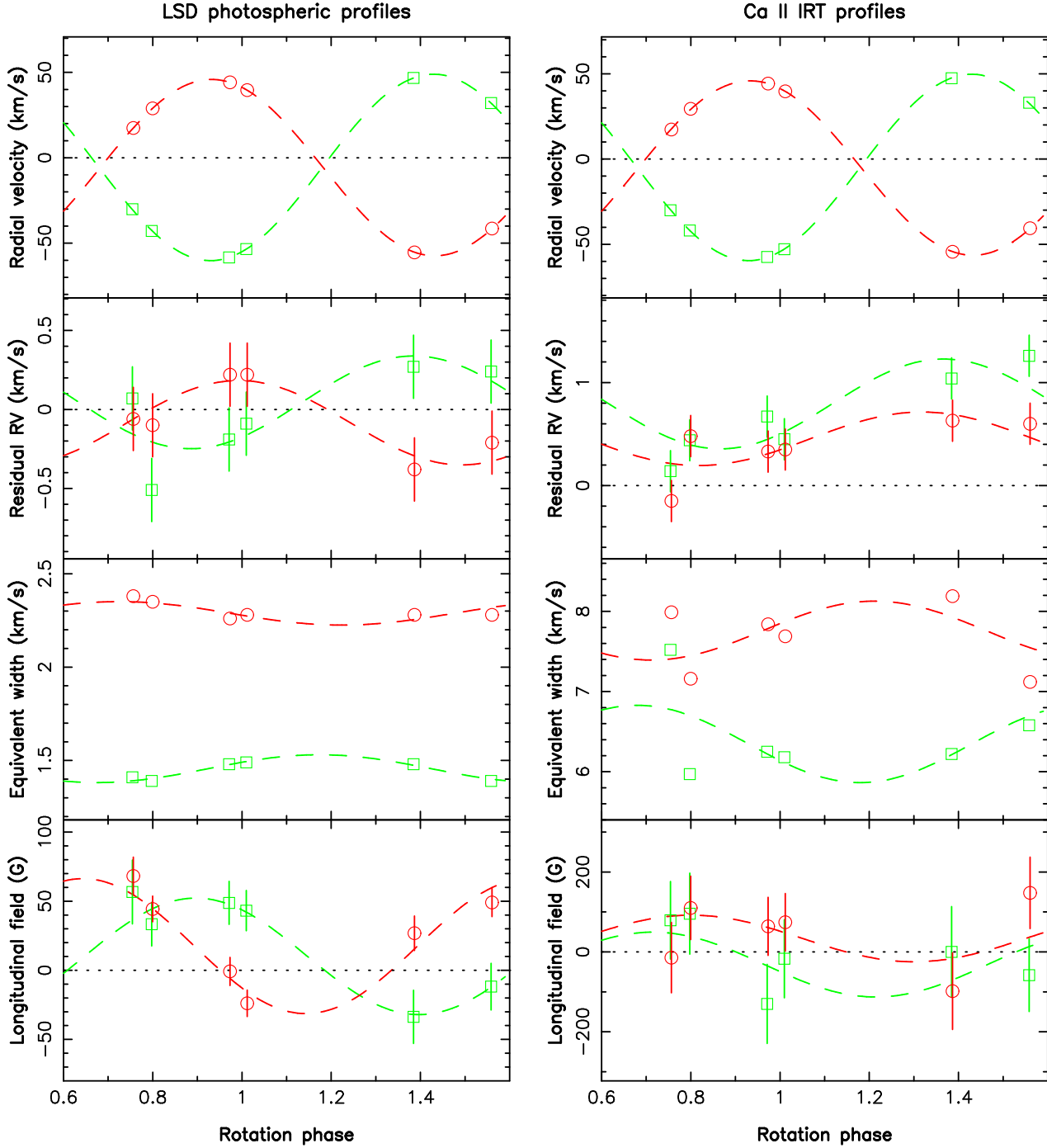


Figure 3. Rotational modulation of the RV (top row), residual RV (second row), equivalent width (third row) and longitudinal field (bottom row) derived from LSD photospheric profiles (left panels) and the average Ca II IRT line (right panels) and for both the primary (red circles) and secondary (green squares) system components of V4046 Sgr. First and second orbital conjunctions respectively occur at phases 0.681 and 0.181 in the ephemeris used here (see Eq. 1). Data collected at near-conjunction epochs and at which spectral contributions of both components overlap and cannot be easily separated from one another (i.e., cycles 1.186 and 3.212) were excluded from this plot. Fits with sine/cosine waves are included (and shown as dashed lines) to outline the amount of variability attributable to rotational modulation (whenever significant), but are not used in the subsequent imaging process. $\pm 1 \sigma$ error bars on data points, based on photon noise only, are also shown whenever larger than symbols.

and hot accretion spots are likely to be located - to be compared later on with the detailed results of the full imaging process (described in the next section). This is what we present in this section; note that the 2 spectra recorded near second conjunction (at cycles 1.186 and 3.212) were

excluded from part of this preliminary analysis, since the contributions of both system components cannot be easily separated from one another.

The main modulation observed in LSD profiles of photospheric lines of V4046 Sgr is the RV shifts resulting from

the orbital motion of both system components; Fig. 2 shows an example profile recorded at cycle 1.972, i.e., slightly after the first quadrature (occurring at phase 0.931, see Sec. 3) and when both components are clearly separated from one another, while Fig. 3 (top left panel) shows the phased RV curves of both components. The orbital elements derived from these profiles (as a by-product of the imaging procedure described in Sec. 5) agree with those of Quast et al. (2000) (except for the significant shift in the phase of first conjunction, see Sec. 3, and for the change in the system velocity, see Sec. 2) but do not support the newer estimates of Stempels & Gahm (2004).

Zeeman signatures are detected at all times in Stokes *V* LSD profiles and in close association with the spectral lines of both components (see Fig. 2 for an example). In most spectra, Stokes *V* signatures are complex, with a typical peak-to-peak amplitudes of 0.2%; they feature several reversals throughout the line profile, suggesting that the parent field topology is not simple. The line-of-sight projected component of the field averaged over the visible stellar hemisphere and weighted by brightness inhomogeneities (called the longitudinal field and estimated from the first moment of the Stokes *V* profile, e.g., Donati et al. 1997) is rather weak (always smaller than 70 G and most of the time smaller than 50 G, with typical error bars of $\simeq 10$ G) and poorly informative about the large-scale field (see Fig. 3 lower left panel).

LSD Stokes *I* profiles also show a small level of rotational modulation (in addition to the RV shifts caused by orbital motion²) as a likely consequence of the presence of cool spots on the stellar surface of both system components (also causing the reported photometric modulation). The line equivalent widths of both system components are observed to vary in anticorrelation and directly reflect the fluctuations in the secondary to primary brightness ratio (around a mean of about 0.64, see Fig. 3 third left panel); the primary star is brightest and/or the secondary star is faintest by a few % around the first orbital conjunction (i.e., phase 0.681) while the opposite holds around the second orbital conjunction (i.e., phase 0.181). Once corrected from the spectral dilution of the companion, the LSD profiles of both system components show equivalent widths of about 3.9 km s^{-1} , fully compatible with those of non-accreting young stars of similar spectral types (e.g., V410 Tau); this demonstrates that veiling was weak (i.e., $< 5\%$) for V4046 Sgr at the time of our observations.

The residual RVs of both system components (in the rest frame of each star, i.e., with the orbital motion removed) is also showing a low-amplitude modulation of $< 1 \text{ km s}^{-1}$ peak to peak, see Fig. 3 second left panel). As the $v \sin i$'s are much larger than the amplitude of this modulation, this suggests in particular the presence of high-latitude spots, around phase 0.2 on the primary star and phase 0.7 on the secondary star, in full agreement with the conclusions

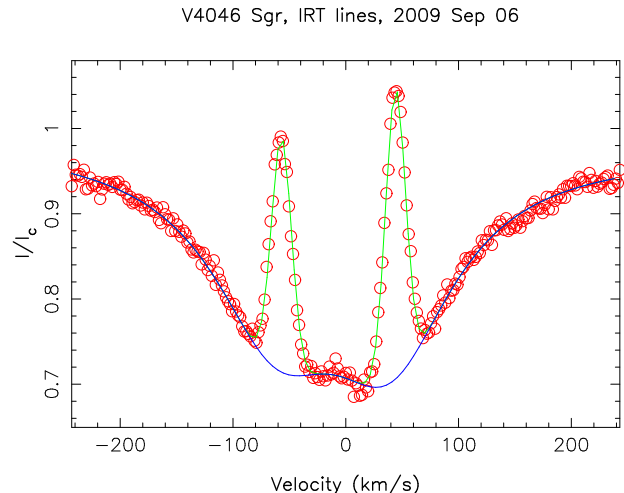


Figure 4. Double Lorentzian fit (bottom blue line) with additional double Gaussian fit (top green line) to the observed mean IRT line profile of V4046 Sgr (red circles) on 2009 Sep 06 (cycle 1.972). The bottom blue line is the background profile model that we subtract from the observed profile to recover the emission profiles of both system components.

derived from the rotational modulation in the equivalent widths of LSD profiles of both components (see above).

We note that LSD Stokes *I* and *V* profiles of both system components repeat well from one rotation cycle to the next, further supporting the conclusion that rotational modulation largely dominates over intrinsic variability in V4046 Sgr, even more than in the moderately accreting cTTS V2129 Oph (Donati et al. 2011a).

As in previous papers, we use core emission in Ca II IRT lines as a proxy of surface accretion even though it usually features a significant (and often dominant) contribution from the non-accreting chromosphere. Previous work (Donati et al. 2010, 2011a) demonstrated in particular that rotational modulation in Stokes *I* and *V* Ca II IRT profiles correlates well with that derived from the more conventional He I D_3 accretion proxy, even for mass accretion rates as low as (or even lower than) that of V4046 Sgr (see below). In the particular case of V4046 Sgr, the emission contributions of both system components are narrow enough to be well separated in velocity during most of the orbital cycle, offering the option of characterizing the accretion behaviour of both stars independently from one another. In practice, we start by constructing a LSD-like weighted average of the 3 IRT lines; we then subtract the underlying (much wider) photospheric absorption profiles, with a single Lorentzian fit to the far line wings when the emission peaks of both system components overlap (i.e., at cycle 1.186 and 3.212, see Sec. 5), and with a double Lorentzian fit to the far wings and the line center when the emission peaks of both system components are well separated in velocity (see Fig. 4 for an example).

The RVs of the emission peaks are fully compatible with the orbital solution derived from photospheric lines (see Fig. 3 top right panel). In the stellar rest frame of each system component, both emission peaks are slightly shifted redwards by about 0.7 km s^{-1} (see Fig. 3 second right panel), as usual in cTTSS and confirming that it traces

² The RV shifts of spectral lines resulting from the orbital motion of both system components were estimated as part of the imaging process (see Sec. 5) and are thus free of contamination from cool surface spots (as opposed to those of Quast et al. 2000); they are thus the most logical ones to use when looking for potential RV signatures of cool surface spots.

slowly-moving regions of the post-shock accretion funnels close to the surface of the star. The equivalent widths of both emission peaks are roughly constant with phase and equal to $\simeq 15 \text{ km s}^{-1}$ or 0.040 nm (once corrected from the spectral dilution) and vary by less than 2 km s^{-1} over the rotation cycle (see Fig. 3 third right panel). It suggests a rather low level of accretion and accretion regions either distributed over the whole visible hemisphere or located very close to the pole (hence producing a very small level of modulation); this is further evidenced by the low-amplitude RV modulation of the emission peaks of both components (once the orbital motion is removed, see Fig. 3 second right panel).

We detect no Zeeman signatures in conjunction with Ca II IRT emission, with error bars on the corresponding longitudinal fields most of the time smaller than 100 G (see Fig. 3 bottom right panel). This is fairly unusual in cTTs, even in those with low mass accretion rates (e.g., Donati et al. 2011a) and suggests that the large-scale fields of both system stars have rather weak dipole components. We nevertheless use the corresponding Stokes V profiles as an additional constraint for the magnetic modelling (see Sec. 5).

Although usually considered as the most reliable accretion proxy, emission in the He I D_3 line at 587.562 nm (not shown here) is hardly usable in the particular case of V4046 Sgr. This is mostly the consequence of the relative weakness of this line in the spectrum of V4046 Sgr and of its significant width (with the contribution of both components overlapping most of the time) - all of this occurring within a relatively crowded spectral region. The best we can obtain is that the total line equivalent width (for both system components as a whole), equal to 17.5 km s^{-1} or 0.034 nm in average, is roughly constant with phase throughout the orbital cycle (in agreement with what the Ca II IRT lines show) except for a (presumably sporadic) emission burst detected at cycle 2.386 (also detected in Balmer lines, see below, but not in Ca II IRT lines). No Zeeman signatures are detected in association with the He I D_3 , consistent with the non-detection in Ca II IRT lines.

Balmer lines are strongly in emission in V4046 Sgr, with widths large enough to blend the contribution of both system components into a single profile (at least for the first few lines of the series). In the particular case of $H\alpha$ and $H\beta$ (see Fig. 5), the total line equivalent widths of the time-averaged profiles are equal to $2,600 \text{ km s}^{-1}$ (5.7 nm) and 475 km s^{-1} (0.77 nm), in line with previous reports (Quast et al. 2000; Stempels & Gahm 2004). The profiles are clearly variable with time but are dominated by intrinsic fluctuations and poorly repeat between consecutive rotational cycles (e.g., cycle 1.186 and 3.212). During our run, we observed in particular a strong short-lived, flare-like burst of emission (e.g., at cycle 2.386), with a conspicuous red-shifted emission component at velocities of up to 350 km s^{-1} suggesting that this event may reflect a short episode of enhanced mass accretion from the disc to the stars. This emission burst is also detected in the He I D_3 line but not in the Ca II IRT nor in the LSD profile of photospheric lines (see Fig. 3 third panels). The width of Balmer lines ($\simeq 200 \text{ km s}^{-1}$ for the full width at half maximum of $H\alpha$, Quast et al. 2000, and $\simeq 400 \text{ km s}^{-1}$ for the full width at 10% height, see below) suggests that it traces free-falling material accelerated from

large distances to the star, possibly from the inner rim of the circumbinary disc.

Although small, we note potential signatures of rotational modulation in both $H\alpha$ and $H\beta$, like for instance the recurrent pseudo-absorption episode detected in the red wing of both lines, at a mean velocity of about 200 km s^{-1} and close to phase 0.8 (at cycles 0.755 and 2.799). Similar (though usually deeper) absorption events are commonly observed in Balmer lines of cTTs (e.g., Bouvier et al. 2007b; Donati et al. 2008b, 2010, 2011a) and are usually interpreted as evidence for accretion veils anchored within the surrounding disc and periodically intersecting the line of sight as the star rotates. In the particular case of V4046 Sgr however, these episodes are only tracing pseudo-absorption (i.e., a lack of emission with respect to the mean profile) rather than true absorption (below the continuum level) and could also potentially be attributed to projection effects in a rotating non-axisymmetric magnetospheric accretion structure. Data with denser phase coverage are necessary to address this issue in more details.

From the average equivalent widths of the Ca II IRT, He I and $H\beta$ lines, we derive logarithmic line fluxes (with respect to the luminosity of the Sun L_\odot) for each star equal to -5.0 , -5.0 and -3.8 respectively³, implying logarithmic accretion luminosities (with respect to L_\odot) of -2.2 , -2.0 and -1.9 respectively (using empirical correlations from Fang et al. 2009). As estimates from the two main accretion proxies (Ca II IRT and He I D_3 lines) agree with each other and with the overall mean, we can safely conclude that the average logarithmic accretion luminosity of each component of V4046 Sgr is -2.0 ± 0.3 and thus that the average logarithmic mass accretion rate of each star in V4046 Sgr (in $M_\odot \text{ yr}^{-1}$) is equal to -9.3 ± 0.3 , with only limited fluctuations around this mean. Our estimate is in good agreement with that of Curran et al. (2011), equal to -9.22 ± 0.23 and also derived from optical lines (though from fully independent data and a different analysis).

Mass accretion rates can in principle also be estimated (though less accurately) through the full width of $H\alpha$ at 10% height (e.g., Natta et al. 2004; Cieza et al. 2010). In the case of V4046 Sgr, $H\alpha$ shows a full width of 420 km s^{-1} in average, implying a logarithmic mass accretion rate estimate of -8.8 ± 0.6 (in $M_\odot \text{ yr}^{-1}$). This is larger (though not very significantly) than the estimate derived from emission fluxes and in agreement with the results of Curran et al. (2011); at this stage, the origin of this potential discrepancy is unclear.

³ To derive line fluxes from normalized equivalent widths, we approximate the continuum level by a Planck function at the temperature of the stellar photosphere. Results are found to be compatible with those in the published literature (e.g., Mohanty et al. 2005) within better than 0.1 dex. In the particular case of V4046 Sgr, we further assume that both stars exhibit more or less the same emission flux, i.e., that the total emission fluxes measured in the spectra reflect (within a factor of $\simeq 2$) that of each system component (in rough agreement with what Ca II IRT lines show, see Sec 5).

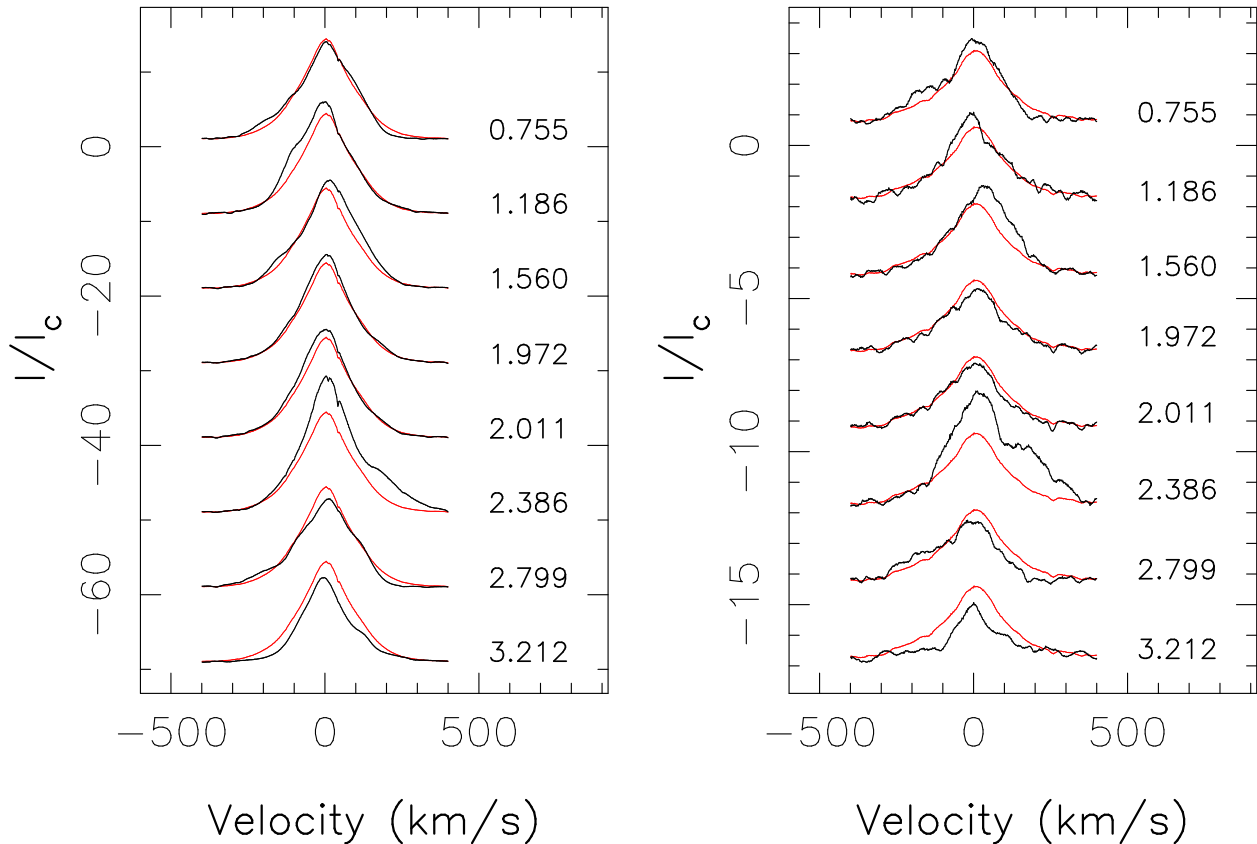


Figure 5. Variation of the H α (left) and H β (right) lines of V4046 Sgr. To emphasize variability, the average profile over the run is shown in red. Orbital/rotation cycles (as listed in Table 1) are mentioned next to each profile.

5 MAGNETIC MODELLING

5.1 Overview of the method

As for the previous papers, we aim at recovering the large-scale field topology of V4046 Sgr, as well as the distribution of surface cool spots and of chromospheric accretion regions, from the collected set of LSD and Ca II IRT profiles presented and described in Secs. 3 and 4. We again apply our new modelling technique (detailed extensively in Donati et al. 2010, 2011a), with the essential difference that we are now aiming at mapping the two stars of the binary system simultaneously.

Following the principles of maximum entropy, our code automatically and simultaneously derives the simplest magnetic topologies, photospheric brightness images and accretion-powered Ca II emission maps compatible with the series of rotationally modulated Stokes I and V LSD and Ca II IRT profiles. The reconstruction process is iterative and proceeds by comparing at each step the synthetic Stokes I and V profiles corresponding to the current images with those of the observed data set. The magnetic field of each star is described through its poloidal and toroidal components expressed as spherical-harmonics (SH) expansions (Donati et al. 2006). The spatial distributions of photospheric brightness (with respect to the quiet photosphere) and those of accretion-powered Ca II emission (in excess of and with respect to that produced by the quiet chromosphere) are modelled as series of independent pixels (typically a few thousand) on a grid covering the visible surfaces

of the stars (with spots in the brightness images assumed to be darker/cooler than the quiet photospheres and spots in the accretion-powered Ca II emission maps supposed to be brighter than the quiet chromospheres).

Synthetic profiles are computed by summing up the elementary spectral contributions from all image pixels over the visible hemispheres of both stars, taking into account the relevant local parameters of the corresponding grid cells (e.g., brightness, accretion-powered excess emission, magnetic field strength and orientation, radial velocity, limb angle, projected area). Since the problem is partly ill-posed, we stabilise the inversion process by using an entropy criterion (applied to the SH coefficients and to the brightness/excess emission image pixels) aimed at selecting the field topologies and images with minimum information among all those compatible with the data. The relative weights attributed to the various SH modes can be imposed, e.g., for purposely producing antisymmetric or symmetric field topologies with respect to the centre of the star (by favouring odd or even SH modes, Donati et al. 2007, 2008b). More details concerning the specific description of local profiles used in the model can be found in Donati et al. (2010).

5.2 Modelling V4046 Sgr

Given the relatively low level of intrinsic variability in the LSD photospheric and Ca II IRT emission lines of V4046 Sgr (see Sec. 4), we applied our imaging model directly to the original profiles without passing them through our usual fil-

tering procedure (aimed at retaining rotational modulation only, see, e.g., Donati et al. 2010, 2011a). We assume that $i = 35$ (see Sec. 2), with values of i ranging from 30° to 40° yielding virtually identical results. We further assume that both stars rotate as solid bodies given the relatively limited coverage and sparse sampling of our data set; assuming Sun-like differential rotation (both in sign and strength, i.e., inducing maximum phase delays of $\pm 3\%$ for the equator and pole with respect to the orbital cycle over the full time span of our observations) generates almost identical images, as expected from the limited spatial resolution available (see below).

The parameters describing the local line profiles on both stars of V4046 Sgr are assumed to be very similar to those used in the previous studies (Donati et al. 2010, 2011a). In particular, the emission profile scaling factor ϵ , describing the emission enhancement of accretion regions over the quiet chromosphere, is again set to $\epsilon = 10$. The local filling factor ψ , describing the relative proportion of magnetic areas at any given point of the stellar surface and set here to $\psi = 1$, has negligible impact on the result given the weak fields detected on V4046 Sgr.

The magnetic, brightness and accretion maps we reconstruct for both stars of V4046 Sgr are shown in Fig. 6, with corresponding fits to the data shown in Fig. 7. The SH expansion describing the field was limited to terms with $\ell \leq 5$; first attempts with $\ell = 8$ indicate that little power is reconstructed in higher order modes ($\ell \geq 6$), reflecting essentially the limited spatial information accessible to Doppler tomography at moderate $v \sin i$ values. For this modelling, we assumed (as in previous studies) that the fields of both stars are antisymmetric (with respect to the stellar centres); this assumption however has little impact on the reconstructed magnetic maps over the visible regions of the stellar surfaces. Our fits reproduce the data down to the noise level, i.e., to a unit reduced chi-square χ_r^2 starting from an initial χ_r^2 of 3.2.

As a by-product, we obtain accurate estimates of the system orbital elements, and in particular of the phase of first conjunction $\phi_0 = 0.6809 \pm 0.0004$, of the velocity amplitude of the primary and secondary components $K_1 = 51.4 \pm 0.2$ and $K_2 = 54.3 \pm 0.2 \text{ km s}^{-1}$, and of the system radial velocity $\gamma = -5.7 \pm 0.2 \text{ km s}^{-1}$. These estimates are in agreement with those of Quast et al. (2000) except for the latter (γ) whose significant variation suggests the presence of a third body in the system. Note in particular that our estimates of K_1 and K_2 are mostly free of contamination from cool surface spots (as opposed to those of Quast et al. 2000) since they are derived as part of the imaging process; we suggest that the small difference between our estimates and those of Quast et al. (2000) (about 0.5 km s^{-1}) mostly reflects the RV signatures of cool surface spots (see Sec. 4 and Fig. 3 left panel second row).

We also find that Ca II lines are redshifted by about 0.7 km s^{-1} with respect to rest frames of both stars, a typical value for cTTSs. In addition, we derive estimates of the projected equatorial rotation velocities $v \sin i$ for both stars, equal to 13.5 ± 0.5 and $12.5 \pm 0.5 \text{ km s}^{-1}$ for the primary and secondary component respectively, as well as a measurement of the magnitude contrast between both system components at the average wavelengths of the LSD and Ca II IRT pro-

files (620 and 850 nm), equal to 0.52 ± 0.10 and 0.22 ± 0.15 respectively⁴.

5.3 Modelling results

The reconstructed large-scale magnetic topologies of both cTTSs in the V4046 Sgr system are weak and multipolar, as expected from the low amplitude and complex shape of the detected Zeeman signatures. On the primary star, the magnetic field has an average surface intensity of $\simeq 230 \text{ G}$, with the azimuthal field component dominating the others and reaching maximum strength ($\simeq 500 \text{ G}$) in conspicuous arc-like structures around the pole; as a consequence, the toroidal field component is found to be very significant, totalling as much magnetic energy as the poloidal component. The poloidal field component is mostly non-axisymmetric, with less than 10% of the energy concentrating in modes with $m < \ell/2$; the dipole (i.e., $\ell = 1$) component has a polar strength of $\simeq 100 \text{ G}$ and is highly tilted (at about 60°) with respect to the rotation axis (pointing towards phase 0.80). On the secondary star, the magnetic field has a comparable average surface intensity (of $\simeq 170 \text{ G}$), with the radial and azimuthal field components of roughly comparable strengths and topologies. The toroidal field component is weaker than in the primary star though still significant, totalling only about 15% of the reconstructed magnetic energy; the poloidal field component is once more mostly non-axisymmetric, with again less than 10% of the energy concentrating in modes with $m < \ell/2$; the dipole component is even weaker ($\simeq 70 \text{ G}$) than on the primary star and is roughly perpendicular to the rotation axis (pointing towards phase 0.1) and to the dipole moment of the primary star.

The photospheric brightness maps we derive for both stars of V4046 Sgr feature one dark spot close to the pole and each covering $\simeq 2\%$ of the stellar surface. Both spots are slightly off-centered (by about $\simeq 10^\circ$) towards phase $\simeq 0.2$ for the primary star and phase $\simeq 0.7$ for the secondary star, i.e., towards the hemisphere that faces the companion star (best viewed from Earth at the orbital phases of the second and first conjunctions, respectively equal to 0.181 and 0.681, see Sec. 3). This is fully consistent with the observed modulation of the LSD profiles of photospheric lines as reported in Sec. 4, showing that the primary is brighter/fainter than the secondary around phases 0.7/0.2 respectively. No obvious correlation between the magnetic and brightness maps, apart from the fact that the (incomplete) counterclockwise ring of azimuthal/toroidal field detected at high latitudes on the primary star is more or less surrounding the corresponding cool polar spot (see Fig. 6 upper panels).

The reconstructed maps of accretion-powered excess emission of both stars mainly show an extended, low-contrast region of enhanced emission centred onto the pole, each covering $\simeq 1\%$ of the stellar surface. Again, this is in agreement with the moderate strength and small (largely insignificant) modulation of the Ca II emission profiles of V4046 Sgr as reported in Sec. 4. As for the brightness maps,

⁴ We speculate that the smaller contrast observed in the Ca II IRT lines reflects the fact that the cooler secondary star is comparatively more active and/or generating more accretion-powered emission than the primary star, by typically 35%.

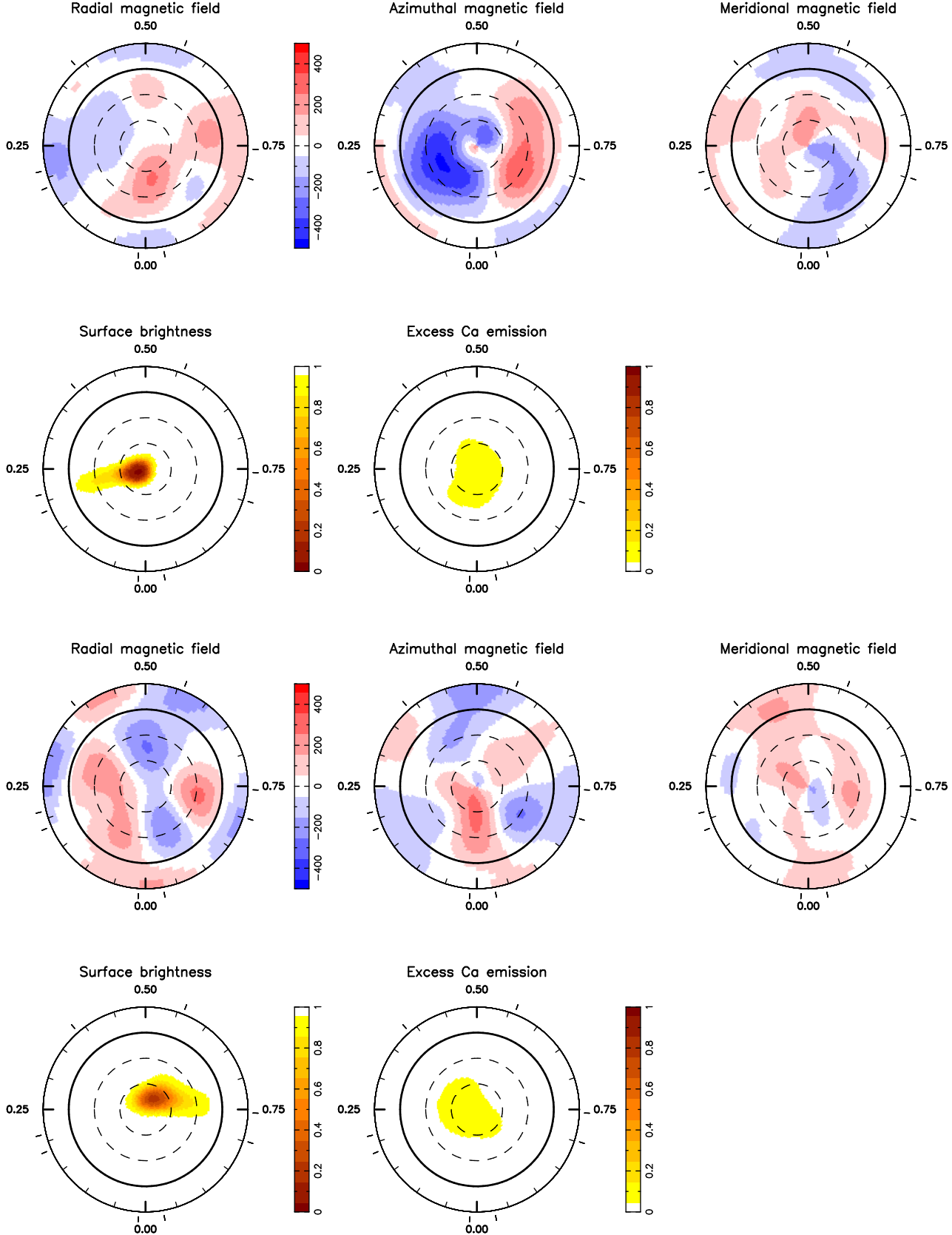


Figure 6. Maps of the radial, azimuthal and meridional components of the magnetic field \mathbf{B} (first and third rows, left to right panels respectively), photospheric brightness and excess Ca II IRT emission (second and fourth rows, first and second panels respectively) at the surface of the primary (top two rows) and secondary (bottom two rows) components of V4046 Sgr. Magnetic fluxes are labelled in G; local photospheric brightness (normalized to that of the quiet photosphere) varies from 1 (no spot) to 0 (no light); local excess Ca II emission varies from 0 (no excess emission) to 1 (excess emission covering 100% of the local grid cell, assuming an intrinsic excess emission of $10\times$ the quiet chromospheric emission). In all panels, the star is shown in flattened polar projection down to latitudes of -30° , with concentric dashed circles representing latitudes of 0° , 30° , and 60° . The radial axis is labeled from 0.00 to 0.50, and the azimuthal axis is labeled from 0.00 to 0.75.

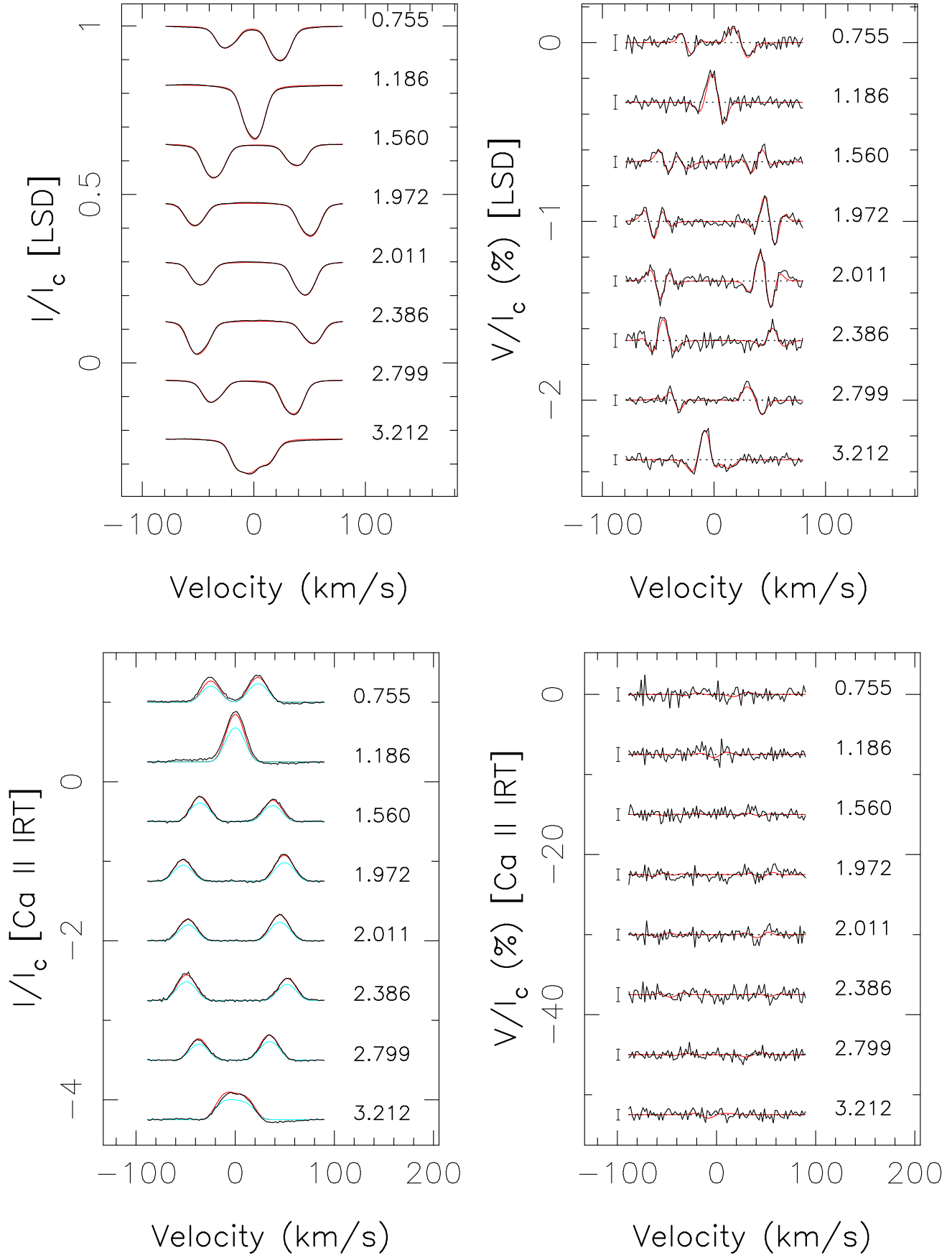


Figure 7. Maximum-entropy fit (thin red line) to the observed (thick black line) Stokes I and Stokes V LSD photospheric profiles (top panels) and Ca II IRT profiles (bottom panels) of V4046 Sgr. The light-blue curve in the bottom left panel shows the (constant) contribution of the quiet chromosphere to the Stokes I Ca II profiles. Orbital/rotational cycles and 3σ error bars (for Stokes V profiles)

we see no obvious connection between these features and the corresponding magnetic maps. We suspect that these extended, low-contrast regions of excess emission centred on the pole may be tracing even more extended features potentially covering most of the star, but with low latitudes truncated by tomographic imaging - the maximum entropy criterion naturally filtering out areas of lowest visibility (i.e., lowest latitudes) when phase sampling and spatial resolution are both moderate (like in the present case). Simulations involving fake stars with properties similar to those of V4046 Sgr (regarding $v \sin i$ and i in particular) and with low-contrast excess emission evenly distributed over the whole surfaces confirm that the reconstructed emission features (centred on the pole) extend no further than latitude 45° typically (i.e., only slightly larger than what we recover in the case of V4046 Sgr) when the quality and sampling of the spectra are similar to those of our observations. Our maps therefore suggest that excess emission likely extends over a large area on both stars of V4046 Sgr, with no more than a small residual excess in the polar regions; new observations with improved phase sampling are needed to validate more firmly this conclusion.

6 SUMMARY & DISCUSSION

Our paper presents new results regarding magnetospheric accretion processes in cTTSs; here we concentrate on the bright cTTS close binary V4046 Sgr, comprised of two $\simeq 12$ Myr-old $\simeq 0.9 M_\odot$ stars separated by 0.041 AU in a 2.42 d-period circular orbit, and observed within the framework of the international multi-wavelength multi-site monitoring campaign organised for this object in 2009 September (involving in particular X-ray observations with XMM-Newton; Argiroffi et al 2011, submitted). Spectropolarimetric data were collected with ESPaDOnS@CFHT over $\simeq 2.5$ orbital/rotation cycles. From these time-resolved spectropolarimetric data and using the latest version of our magnetic tomographic imaging code (extended to the case of close double-line binaries), we reconstruct maps of the large-scale magnetic field, of the photospheric brightness and of the accretion-powered Ca II IRT excess emission at the surface of both the primary and secondary stars of V4046 Sgr.

The large-scale fields of both stars are found to be weak and complex (with respect to those of other cTTSs of similar masses in particular), with average field strengths of typically $\simeq 200$ G, a highly non-axisymmetric poloidal component, and a significant toroidal component; in particular, the large-scale dipole field components are weak (100 and 70 G for the primary and secondary star respectively), highly tilted with respect to the rotation axis and perpendicular to each other. This is radically different from the strong, mainly poloidal, mostly axisymmetric magnetic topologies of prototypical cTTSs such as BP Tau or AA Tau (Donati et al. 2008b, 2010), and similar to field configurations of more massive cTTSs (e.g., Hussain et al. 2009). The field configurations of both cTTSs of V4046 Sgr are also quite similar to those found in HD 155555 (another slightly more massive close binary of the β Pic moving group, see Sec. 2), also showing a weak and complex field with a highly non-axisymmetric poloidal component and a significant toroidal component (Dunstone et al. 2008).

By analogy with dynamo-generated magnetic topologies of main-sequence stars, we speculate that this contrast reflects a drastic difference in the internal structure of the star, with fully-convective stars (those not too far below the full-convection limit at least) showing strong, mostly axisymmetric and poloidal magnetic configurations and partly-convective stars exhibiting much weaker and more complex poloidal fields and a significant toroidal component (Donati & Landstreet 2009). Given their likely age of $\simeq 12$ Myr, the components of V4046 Sgr should belong to the second category while BP Tau and AA Tau belong to the first, further strengthening the conclusion that magnetic fields of cTTSs have a dynamo origin (e.g., Donati et al. 2011a).

Our images also show that both stars of V4046 Sgr host cool spots close to the pole, similar to (though smaller in size than) those mapped at the surface of HD 155555 (Dunstone et al. 2008); we also find that, for each star in the system, these spots are slightly off-centred towards the hemisphere that faces the companion star, in agreement with the primary star being brighter and fainter than the secondary star (as judged from the primary to secondary line depth ratio, see Sec. 4 and Fig. 3) at orbital phases of first and second conjunction respectively (i.e., phases 0.681 and 0.181 respectively). We find no clear correlation between the reconstructed brightness maps and corresponding magnetic topologies, despite both being reconstructed simultaneously in a fully self-consistent way; in particular, the cool polar spots are apparently not coincident with one pole of a mainly axisymmetric magnetic topology as in most other cTTSs (Donati et al. 2008b, 2010, 2011a). The only connection we can report between magnetic topologies and photospheric brightness maps is that the (incomplete) unipolar ring of counterclockwise azimuthal field detected on the primary star is encircling the cool polar spot; this is very similar to what is reported for rapidly-rotating partly-convective solar-type stars (e.g., Donati et al. 2003; Dunstone et al. 2008).

The maps of accretion-powered excess emission we recover for both stars from sets of Ca II IRT profiles show a low-contrast, extended feature centred on the pole, directly reflecting the low emission and small modulation that the Ca II IRT lines exhibit (see Sec. 4 and Fig. 3). In particular, these maps are less contrasted than those of most other cTTSs imaged to date (Donati et al. 2010, 2011a) despite a similar mass accretion rate (of -9.3 ± 0.3 in logarithmic scale and in $M_\odot \text{ yr}^{-1}$, see Sec. 4); they also show no obvious resemblance with the corresponding magnetic maps. Tomographic imaging simulations suggest that the parent distributions of excess emission at the surfaces of both stars of V4046 Sgr may potentially cover the whole surfaces (with signal from low latitudes being filtered out by the maximum entropy criterion) and no more than a low-contrast residual emission excess close to the pole.

We suggest that this reflects that accretion onto each star of V4046 Sgr does not concentrate into a single specific region of the visible hemisphere (as it does on other cTTSs, e.g., Donati et al. 2008b, 2010, 2011a) but rather occurs simultaneously at several places over the whole stellar surface; in each of the individual accretion sites, mass accretion is presumably not high enough to produce distinct features in the maps of accretion-powered emission excesses, especially given the limited spatial resolution achievable at the surfaces

of both stars of V4046 Sgr. Any residual low-contrast excess emission close to the pole may indicate that chromospheric emission is not homogeneous on both stars of V4046 Sgr (as originally assumed in the model) but is slightly stronger at high latitudes, where cool spots are observed to cluster at photospheric level.

Distributed accretion is consistent with the fact that the dipolar components of the large-scale fields of both stars are weak and that the field topology within the magnetospheric gap (extending no further than $0.5\text{--}1 R_*$ above the surface of both components of V4046 Sgr) is complex, dominated by higher-order terms of the magnetic spherical expansions and thus featuring multiple poles over the visible hemisphere. The red-shifted pseudo-absorption episodes potentially observed in Balmer lines at specific phases (rather than throughout the whole rotation cycle, see Sec. 4) may provide more information about the spatial intermittency of accretion funnels, if further data (with much denser phase coverage) demonstrate that these episodes are reliable probes of accretion funnels crossing the line of sight in V4046 Sgr as well.

Recent 2D and 3D numerical hydrodynamical simulations of mass accretion onto close cTTS binaries (Kaigorodov et al. 2010; Fateeva et al. 2011; de Val-Borro et al. 2011) suggest that accretion may not directly proceed from the circumbinary disc to the stars; more specifically, they find that local small-size discs may develop around both stars, with material flowing from the circumbinary disc to the small discs through the circumbinary gap (and in particular through the co-rotating outer Lagrange points), and forming a double-armed spiral structure (with one arm joining each local disc to the wider circumbinary disc) as well as a bridge connecting both local discs. The local discs have predicted sizes similar to those of the corresponding Roche lobes, with radii of $\simeq 3 R_*$ in the particular case of V4046 Sgr. Observations of optically-thin Balmer lines however suggest that only the accretion streams actually exist in V4046 Sgr and not the local discs, as a possible result of them being magnetically disrupted by the large-scale fields of both stars (de Val-Borro et al. 2011).

Self-consistent simulations including the effects of magnetic fields are not available yet. As of now, our results suggest that the large-scale fields of both stars, and in particular their dipolar components, are likely not strong enough to disrupt the predicted local discs around both system stars beyond a typical distance of $1 R_*$ above the stellar surfaces. However, our data can neither directly confirm nor invalidate the existence of local accretion discs. For instance, the Ca II IRT emission components, although a useful tracer of the hot footpoints at the base of accretion funnels, show no evidence of accretion spots located beyond the surfaces of the system stars, e.g., where the spiral accretion streams supposedly meet the putative local accretion discs; it is however not clear from the existing simulations whether such spots truly exist and, if they do, whether they are bright enough to be detected.

The time-resolved contemporaneous (though not exactly simultaneous) X-ray observations of V4046 Sgr collected with XMM-Newton in the framework of our international campaign can provide useful constraints onto magnetospheres and accretion processes in a close cTTS binary like

V4046 Sgr. They confirm in particular that the X-ray emission measure distribution of V4046 Sgr is similar to that of the evolved cTTS TW Hya, featuring in particular a hard X-ray component of coronal origin (with plasma temperatures of up to 10 MK) and a soft X-ray one (with an average temperature of about 3 MK) presumably probing the accretion shocks at the base of accretion funnels (Argiroffi et al. 2011, submitted). That TW Hya hosts a strong and mostly axisymmetric large-scale magnetic field (Donati et al. 2011b) drastically different from those of both stars of V4046 Sgr makes this similarity very intriguing and even more interesting to study.

At least three major flares in the hot X-ray component were monitored (including both the rise and decay phases) during these observations, suggesting flaring loops with maximum sizes comparable to the stellar radii (Maggio et al. 2011, in preparation); this is in good agreement with our independent conclusion that the magnetospheres of both stars in V4046 Sgr do not extend beyond $1 R_*$ above the surface of the star. Since rotation and orbital motion are locked in V4046 Sgr, and given that the distance between both system components ($\simeq 8.8 R_*$) is much larger than the reported loop sizes and magnetospheres, this flaring activity is unlikely caused by interacting magnetospheres (as proposed for DQ Tau, Getman et al. 2011) but is rather attributable to conventional coronal activity similar to that observed on most active Sun-like stars and presumably triggered by differential rotation at the surface of both stars mostly (rather than to rapid changes in the surface magnetic topologies themselves).

Obviously, more work is required, both on the observational and theoretical sides, to understand how magnetospheric accretion processes work in the case of close cTTS binaries, and in particular how they differ from those occurring in single cTTSs. Coordinated multi-wavelength campaigns like that organized for V4046 Sgr and described in the present and forthcoming papers, are crucial in this respect, and need to be carried out for binary stars of different masses, rotation/orbital rates and ages.

ACKNOWLEDGEMENTS

We thank an anonymous referee for comments that improved the manuscript. This paper is based on observations obtained at the Canada-France-Hawaii Telescope (CFHT), operated by the National Research Council of Canada, the Institut National des Sciences de l'Univers of the Centre National de la Recherche Scientifique of France and the University of Hawaii. The “Magnetic Protostars and Planets” (MaPP) project is supported by the funding agencies of CFHT and TBL (through the allocation of telescope time) and by CNRS/INSU in particular, as well as by the French “Agence Nationale pour la Recherche” (ANR). SHPA acknowledges financial support from Fapemig, CAPES and COFECUB.

REFERENCES

André P., Basu S., Inutsuka S., 2009, The formation and evolution of prestellar cores. Cambridge University Press,

- p. 254
- Applegate J. H., 1992, *ApJ*, 385, 621
- Bouvier J., Alencar S. H. P., Boutelier T., Dougados C., Balog Z., Grankin K., Hodgkin S. T., Ibrahimov M. A., Kun M., Magakian T. Y., Pinte C., 2007b, *A&A*, 463, 1017
- Bouvier J., Alencar S. H. P., Harries T. J., Johns-Krull C. M., Romanova M. M., 2007a, in Reipurth B., Jewitt D., Keil K., eds, *Protostars and Planets V Magnetospheric Accretion in Classical T Tauri Stars*. pp 479–494
- Cieza L. A., Schreiber M. R., Romero G. A., Mora M. D., Merin B., Swift J. J., Orellana M., Williams J. P., Harvey P. M., Evans N. J., 2010, *ApJ*, 712, 925
- Curran R. L., Argiroffi C., Sacco G. G., Orlando S., Peres G., Reale F., Maggio A., 2011, *A&A*, 526, A104
- da Silva L., Torres C. A. O., de La Reza R., Quast G. R., Melo C. H. F., Sterzik M. F., 2009, *A&A*, 508, 833
- de Val-Borro M., Gahm G. F., Stempels H. C., Pepliński A., 2011, *MNRAS*, 413, 2679
- Donati J., Bouvier J., Walter F. M., Gregory S. G., Skelly M. B., Hussain G. A. J., Flaccomio E., Argiroffi C., Grankin K. N., Jardine M. M., Ménard F., Dougados C., Romanova M. M., 2011a, *MNRAS*, 412, 2454
- Donati J., Gregory S., Alencar S., Bouvier J., Hussain G., Skelly M., Dougados C., Jardine M., Menard F., Romanova M., Unruh Y., the MaPP collaboration 2011, *MNRAS* in press (arXiv:1106.4162)
- Donati J., Landstreet J. D., 2009, *ARA&A*, 47, 333
- Donati J., Skelly M. B., Bouvier J., Gregory S. G., Grankin K. N., Jardine M. M., Hussain G. A. J., Ménard F., Dougados C., Unruh Y., Mohanty S., Aurière M., Morin J., Farès R., 2010, *MNRAS*, 409, 1347
- Donati J.-F., 2003, in Trujillo-Bueno J., Sanchez Almeida J., eds, *Astronomical Society of the Pacific Conference Series Vol. 307 of Astronomical Society of the Pacific Conference Series, ESPaDOnS: An Echelle SpectroPolarimetric Device for the Observation of Stars at CFHT*. p. 41
- Donati J.-F., Cameron A., Semel M., Hussain G., Petit P., Carter B., Marsden S., Mengel M., Lopez Ariste A., Jeffers S., Rees D., 2003, *MNRAS*, 345, 1145
- Donati J.-F., Howarth I. D., Jardine M. M., Petit P., Catala C., Landstreet J. D., Bouret J.-C., Alecian E., Barnes J. R., Forveille T., Paletou F., Manset N., 2006, *MNRAS*, 370, 629
- Donati J.-F., Jardine M. M., Gregory S. G., Petit P., Bouvier J., Dougados C., Ménard F., Cameron A. C., Harries T. J., Jeffers S. V., Paletou F., 2007, *MNRAS*, 380, 1297
- Donati J.-F., Jardine M. M., Gregory S. G., Petit P., Paletou F., Bouvier J., Dougados C., Ménard F., Cameron A. C., Harries T. J., Hussain G. A. J., Unruh Y., Morin J., Marsden S. C., Manset N., Aurière M., Catala C., Alecian E., 2008b, *MNRAS*, 386, 1234
- Donati J.-F., Moutou C., Farès R., Bohlender D., Catala C., Deleuil M., Shkolnik E., Cameron A. C., Jardine M. M., Walker G. A. H., 2008a, *MNRAS*, 385, 1179
- Donati J.-F., Semel M., Carter B. D., Rees D. E., Collier Cameron A., 1997, *MNRAS*, 291, 658
- Dunstone N. J., Hussain G. A. J., Collier Cameron A., Marsden S. C., Jardine M., Stempels H. C., Ramirez Velez J. C., Donati J.-F., 2008, *MNRAS*, 387, 481
- Fang M., van Boekel R., Wang W., Carmona A., Sicilia-Aguilar A., Henning T., 2009, *A&A*, 504, 461
- Fateeva A. M., Bisikalo D. V., Kaygorodov P. V., Sytov A. Y., 2011, *Ap&SS*, p. 29
- Favata F., Micela G., 2003, *SSRv*, 108, 577
- Feigelson E. D., Montmerle T., 1999, *ARA&A*, 37, 363
- Getman K. V., Broos P. S., Salter D. M., Garmire G. P., Hogerheijde M. R., 2011, *ApJ*, 730, 6
- Gregory S. G., Jardine M., Gray C. G., Donati J., 2010, *Reports on Progress in Physics*, 73, 126901
- Güdel M., Nazé Y., 2009, *A&AR*, 17, 309
- Günther H. M., Liefke C., Schmitt J. H. M. M., Robrade J., Ness J., 2006, *A&A*, 459, L29
- Hussain G. A. J., Collier Cameron A., Jardine M. M., Dunstone N., Velez J. R., Stempels H. C., Donati J.-F., Semel M., Aulanier G., Harries T., Bouvier J., Dougados C., Ferreira J., Carter B. D., Lawson W. A., 2009, *MNRAS*, p. 997
- Hut P., 1981, *A&A*, 99, 126
- Johns-Krull C. M., 2007, *ApJ*, 664, 975
- Kaigorodov P. V., Bisikalo D. V., Fateeva A. M., Sytov A. Y., 2010, *Astronomy Reports*, 54, 1078
- Kurucz R., 1993, *CDROM # 13 (ATLAS9 atmospheric models) and # 18 (ATLAS9 and SYNTHE routines, spectral line database)*. Smithsonian Astrophysical Observatory, Washington D.C.
- Lanza A. F., 2006, *MNRAS*, 369, 1773
- Mentuch E., Brandeker A., van Kerkwijk M. H., Jayawardhana R., Hauschildt P. H., 2008, *ApJ*, 689, 1127
- Mohanty S., Jayawardhana R., Basri G., 2005, *ApJ*, 626, 498
- Natta A., Testi L., Muzerolle J., Randich S., Comerón F., Persi P., 2004, *A&A*, 424, 603
- Quast G. R., Torres C. A. O., de La Reza R., da Silva L., Mayor M., 2000, in *IAU Symposium Vol. 200 of IAU Symposium, V4046 Sgr, a key young binary system..* p. 28P
- Rodriguez D. R., Kastner J. H., Wilner D., Qi C., 2010, *ApJ*, 720, 1684
- Siess L., Dufour E., Forestini M., 2000, *A&A*, 358, 593
- Stempels H. C., Gahm G. F., 2004, *A&A*, 421, 1159
- Torres C. A. O., Quast G. R., Melo C. H. F., Sterzik M. F., 2008, *Young Nearby Loose Associations*. p. 757
- Yee J. C., Jensen E. L. N., 2010, *ApJ*, 711, 303
- Zahn J.-P., Bouchet L., 1989, *A&A*, 223, 112